Journal of Vacuum Science and Technology A

RESEARCH ARTICLE | MARCH 29 2024

Comparison of three titanium-precursors for atomic-layer-deposited TiO_2 for passivating contacts on silicon

Special Collection: Atomic Layer Deposition (ALD)

Daniel Hiller ; Frans Munnik ; Julian López-Vidrier ; Dmytro Solonenko ; Johanna Reif; Martin Knaut ; Oliver Thimm; Nicholas E. Grant

J. Vac. Sci. Technol. A 42, 032406 (2024)
https://doi.org/10.1116/6.0003309

JVST A
Journal of Vacuum Science & Technology A

ARTICLE

pubs.aip.org/avs/jva

Comparison of three titanium-precursors for atomic-layer-deposited TiO_2 for passivating contacts on silicon

Cite as: J. Vac. Sci. Technol. A 42, 032406 (2024); doi: 10.1116/6.0003309
Submitted: 17 November 2023 · Accepted: 5 March 2024 ·
Published Online: 29 March 2024

Daniel Hiller,[1,2,3,a)] Frans Munnik,[4] Julian López-Vidrier,[5] Dmytro Solonenko,[6] Johanna Reif,[2] Martin Knaut,[2] Oliver Thimm,[7] and Nicholas E. Grant[8]

AFFILIATIONS

[1]Institute of Applied Physics (IAP), TU Bergakademie Freiberg, 09599 Freiberg, Germany
[2]Chair of Nanoelectronics, Institute of Semiconductors and Microsystems (IHM), Technische Universität Dresden, 01187 Dresden, Germany
[3]Research School of Engineering, Australian National University (ANU), Canberra, ACT 2601, Australia
[4]Institute of Ion Beam Physics and Materials Research, Helmholtz-Zentrum Dresden-Rossendorf (HZDR), 01328 Dresden, Germany
[5]Departament de Física Aplicada, Universitat de Barcelona, 08028 Barcelona, Spain
[6]Semiconductor Physics Research Group, Technische Universität Chemnitz, 09126 Chemnitz, Germany
[7]IEK-5 Photovoltaik, Forschungszentrum Jülich, 52425 Jülich, Germany
[8]School of Engineering, University of Warwick, Coventry CV4 7AL, United Kingdom

Note: This paper is part of the 2024 Special Topic Collection on Atomic Layer Deposition (ALD).
[a)]**Author to whom correspondence should be addressed:** daniel.hiller@physik.tu-freiberg.de

ABSTRACT

Atomic layer-deposited (ALD) TiO_2 thin films on silicon were deposited using titanium tetrachloride ($TiCl_4$), titanium tetraisopropoxide (TTIP), and tetrakis(dimethylamino)titanium (TDMAT) together with water vapor as the oxidant at temperatures ranging between 75 and 250 °C. The Si surface passivation quality of as-deposited and isothermally annealed samples was compared using photoconductance lifetime measurements in order to calculate their effective surface recombination velocities S_{eff}. A low S_{eff} of 3.9 cm/s ($J_{0s} = 24$ fA/cm^2) is achieved for as-deposited $TiCl_4$-TiO_2 at 75 °C when a chemically grown (i.e., from RCA cleaning) SiO_x interface layer is present. Depositing TTIP-TiO_2 at 200 °C on a chemically grown SiO_x interface layer yields equivalent S_{eff} values; however, in this case, TTIP-TiO_2 requires a 5–15 min postdeposition forming gas anneal at 250 °C. In contrast, TDMAT-TiO_2 was not found to provide a similar level of passivation with/without a chemically grown SiO_x interface layer and postdeposition anneal. Modeling of the effective lifetime curves was used to determine the magnitude of the effective charge densities Q_f in the TiO_2 films. In all cases, Q_f was found to be of the order of $\sim 10^{11}$ q cm^{-2}, meaning field-effect passivation arising from ALD TiO_2 is relatively weak. By comparing the material properties of the various TiO_2 films using ellipsometry, photothermal deflection spectroscopy, Raman spectroscopy, elastic recoil detection analysis, x-ray photoelectron spectroscopy, and Fourier transform infrared spectroscopy, we find experimental support for the role of Cl (in conjunction with hydrogen) playing a beneficial role in passivating dangling bond defects at the Si surface. It is concluded that low deposition temperature $TiCl_4$ processes are advantageous, by providing the lowest S_{eff} without any postanneal and a comparatively high growth per cycle (GPC).

I. INTRODUCTION

Silicon photovoltaics (PV) is one of the cheapest electricity generation technologies and is free of greenhouse gas emissions during the time of power generation with a short carbon payback period concerning the emissions from PV manufacturing. Therefore, PV deployment continues to grow at high annual rates in many parts of the world.[1] Currently, the passivated emitter and rear (PERC) solar cell is the dominant cell technology, whereby the metal-semiconductor contact area at the rear surface is drastically reduced compared to the full-area aluminum back surface field (Al-BSF) design.[2] It is envisaged for many future PV technologies that interlayers will avoid any direct contact between the crystalline silicon and the contact metal to further reduce recombination. For some of these solar cell concepts, carrier-selective passivating contacts are investigated, in which ultrathin dielectrics or wide-bandgap semiconductors play a crucial role.[3,4]

Titanium dioxide (TiO_2) grown by atomic layer deposition (ALD) is a material that provides a very high level of surface passivation on *n*-type and *p*-type silicon wafers.[5,6] In addition, the high refractive index of TiO_2 (~2.4 at 633 nm) makes ~60 nm thick films an efficient single-layer antireflective coating (ARC) due to the high transparency of the film resulting from its wide bandgap (~3.3 eV).[7] Apart from these favorable optical properties, which dominate for thicker films, ALD TiO_2 has also favorable electronic properties, rendering ultrathin films a potential passivating contact material. The nearly aligning conduction bands of TiO_2 and Si, combined with the natural *n*-type doping of ALD TiO_2, shape this material as an electron-selective contact, especially when combined with a mid/low work function metal (e.g., Al, Ca, and Mg).[8–13] In contrast, Matsui *et al.* demonstrated a passivating hole-selective contact when combining ALD TiO_2 with a high work function metallization.[14,15] Recently, mixed TiO_x-AlO_y layers and other film stack combinations, including, e.g., LiF or ZnO, were proposed as passivating contact materials.[16,17] Furthermore, TiO_2 was suggested as a junction material in perovskite/Si tandem cells.[18]

The frequently observed excellent Si surface passivation from ALD TiO_2 is based on two main factors that suppress electron-hole recombination on the Si surface, namely, the chemical passivation and (as introduced by Cuevas[4] *et al.*) the carrier population control. The former is a result of the inevitable ALD in situ growth of an ultrathin interface silicon oxide (SiO_x) and subsequent mixed SiO_x-TiO_x near-interfacial layer[19] in combination with hydrogen species from ALD TiO_2 that can passivate Si dangling bond defects at the Si/SiO_x interface very well.[9,20,21] Moreover, several studies revealed that the intentional (thermal or wet-chemical) growth of an interfacial SiO_x layer before the ALD process improves the Si surface passivation quality.[8–10,12,22] The latter, i.e., carrier population control, can be mediated by fixed charges in the dielectric that cause a strongly asymmetric population of electrons and holes near the Si surface, which is also referred to as field effect passivation. For ALD TiO_2, the presence of a medium density of negative fixed charges was proposed.[6,7,23] However, the precise characterization of fixed charges by conventional capacitance-voltage or contactless corona-voltage measurements is often impeded by the transconductance through the leaky TiO_2 films.[6,7]

Considering the substantial progress with ALD TiO_2 as passivating contact material reported in the literature, it may appear surprising that no consensus prevails about the best choice of the ALD Ti precursor. TiO_2 can be deposited using several Ti precursors, and over 50 different ALD routes exist.[24] The three dominant Ti precursors used for Si surface passivation are titanium tetrachloride ($TiCl_4$),[5–8,16,17,19,25] titanium tetraisopropoxide {$Ti[OCH(CH_3)_2]_4$ (TTIP)},[9,11,15,16,26] and tetrakis(dimethylamino)titanium {$Ti[N(CH_3)_2]_4$, (TDMAT)}.[10,12,13,21,22,27] Since plasma-enhanced ALD of TiO_2 was shown to provide no reasonable Si surface passivation,[28] we chose to focus on thermal ALD in this study and attempt to provide a comparison of these three Ti precursors concerning their passivation quality and TiO_2 material properties.

II. EXPERIMENTAL

TiO_2 thin films using Ti precursors titanium tetrachloride ($TiCl_4$) and titanium tetraisopropoxide (TTIP) were deposited in a Beneq TFS 200 ALD system. For the TiO_2 thin films using tetrakis(dimethylamino)titanium (TDMAT), a Cambridge NanoTech Savannah-100 system was used. Water vapor was the oxidant and N_2 was the purge gas for all processes. The ALD process parameters are listed in Table I.

Surface passivation was studied on front- and backside deposited, ⟨100⟩-oriented, shiny etched, 100 mm diameter, FZ-Si wafers with 5 Ω cm (*n*-type, ~400 μm thick) and 2.5 Ω cm (*p*-type, ~300 μm thick) using one sample per Ti precursor and deposition temperature. Due to the low temperature of deposition and postannealing, the FZ-Si wafers did not receive any initial defect annihilation annealing since no bulk-lifetime degradation is induced at temperatures ≤250 °C.[29–31]

Mirror-polished Cz–Si substrates (~5 Ω cm, *n*-type and *p*-type) were used for ellipsometry, electrical measurements, elastic recoil detection analysis (ERDA), x-ray photoelectron spectroscopy (XPS), and Fourier transform infrared spectroscopy (FTIR). Raman spectroscopy and photothermal deflection spectroscopy (PDS) were used to measure TiO_2 films deposited onto double-side polished quartz glass substrates. All substrates received a complete RCA cleaning prior to ALD including HF dip (~1%). The respective lifetime samples are labelled "HF-last." For one additional set of

TABLE I. ALD process parameters of ALD TiO_2. The growth per cycle (GPC) values of these processes can be found in Fig. 4.

Ti precursor	Ti precursor temperature (°C)	Ti pulse (s)	Ti purge (s)	H_2O pulse (s)	H_2O purge (s)	Deposition temperatures (°C)
$TiCl_4$	Room temp., vapor draw	0.05	0.75	0.05	0.75	75, 150, 200, 250
TTIP	40 °C, bubbler	1.0	2.0	0.5	4.0	150, 200, 250
TDMAT	75 °C, vapor draw	0.1	2.5	0.025	2.5	150, 200, 250

lifetime samples, the final HF dip was omitted, leaving an approximately 1.2 nm thick oxide on the surface that was grown by the RCA-2 solution (labelled "RCA-last"). This allows studying the influence of an intentionally pregrown interfacial silicon oxide with the Si-passivation quality. Isothermal forming gas anneals (FGA) at 250 °C for cumulative durations of 5–60 min were carried out in a tube furnace at a flow of ∼200 l/h of 5% H_2 in Ar.

The effective minority carrier lifetimes τ_{eff} were measured using a Sinton Instruments WCT-120 photoconductance tool. The effective surface recombination velocity S_{eff} at an injection level of 10^{15} cm^{-3} was calculated via $S_{eff} = \frac{W}{2}\left(\frac{1}{\tau_{eff}} - \frac{1}{\tau_{bulk}}\right)$, where W is the wafer thickness and τ_{bulk} is the intrinsic bulk lifetime. The surface saturation current density J_{0s} was extracted using the Kane–Swanson method. Modeling of the measured effective lifetime over excess carrier density was used to separate the passivation components arising from chemical and field effect passivation, which allows us to extract the fixed charge density Q_f of the different ALD TiO_2 layers.[32,33] To model the lifetime curves, we use a method proposed by Girisch *et al.*[34] and extended by Aberle *et al.*,[35] whereby the interface recombination is assumed to be dominated by a single defect at mid-gap. We assume an equal electron σ_n and hole σ_p capture cross section of 10^{-16} cm^2 and we vary the interface defect density and Q_f to accurately model the lifetime curves. In the case of modelling Q_f, we assume a negative polarity as demonstrated in previous studies and the extracted values of Q_f are lower limits only.[4,23] We account for intrinsic recombination using the parameterization by Niewelt[36] *et al.* and estimate the bulk lifetime by passivating a bare, uncoated *n*-type FZ-Si sample using a room-temperature superacid treatment.[31,37,38] TiO_2 film thickness and optical constants were derived from variable angle spectroscopic ellipsometry (VASE; J.A. Woollam M-2000D) from 400 to 1000 nm and at angles of 65°, 70°, and 75°. TiO_2 was modelled using an extended Cauchy model as well as a TiO_2 Tauc–Lorentz model for comparison. For contact resistivity measurements, ten circular contacts of 350 nm Al with varying diameters from 1 to 7 mm (Cox-and-Strack pattern)[39] were thermally evaporated through a shadow mask on the front side. A full-area ohmic substrate contact was made by a Ga–In eutectic alloy. Current-voltage (I-V) measurements were made with a Keithley 2425 source meter. Due to the nonohmic I-V curves, resistance values R at 40 mA/cm^2 (typical maximum power point current density of a full area contact) were fitted against the contact diameter d via $R = \frac{\rho}{\pi d}\arctan\left(\frac{4t}{d}\right) + \frac{4\rho_c}{\pi d^2} + R_0$, where ρ is the substrate resistivity, t is the substrate thickness, ρ_c is the contact resistivity, and R_0 is the back contact resistance.[39] The stoichiometry and impurities in ALD TiO_2 were quantified by time-of-flight (ToF-) ERDA using a 15 MeV (Ref. 35) Cl^{4+} ion beam at an incident angle of 70° to the sample normal and with a scattering angle of 39.9° or ERDA with a 43 MeV (Ref. 35) Cl^{7+} ion beam at an incident angle of 75° to the sample normal and a Bragg ionization chamber (BIC) as detector at a scattering angle of 40°. The analyzed sample area was approximately 2×2 mm^2. The analysis was performed with Potku v2.0[40] for ToF-ERDA and with ndf v9.3g[41] for BIC-ERDA. XPS (Scienta Omicron) was measured using an Al-Kα source (1486.6 eV), an electron emission angle of 45°, and a pass energy of 30 eV. Binding energies were calibrated using the C 1s peak of ambient hydrocarbons (at 285 eV). In order to study the interfacial SiO_x layer, polarized Brewster-angle reflection FTIR was carried out using Bruker VERTEX 80v with p-polarized light and the sample holder at 76°. As shown recently,[42] this FTIR method allows us to eliminate Si-substrate interference fringes and enhances the longitudinal optical (LO) phonon signals from the symmetric Si–O stretching mode. For Raman measurements, a Horiba Jobin-Yvon LabRam spectrometer equipped with a 100× objective and a 532 nm laser was used. The weak Raman background signals from the quartz glass substrates were subtracted. The PDS measurements were performed by using two light sources in order to achieve a broader wavelength region. The combination of a xenon bulb (OSRAM XBO 150 W, ORIEL 68806 Basic Power Supply) and a halogen bulb (OSRAM HLX 100 W, HEINZINGER Power supply PTN 16–10) allows measurements from 310 up to 2600 nm. The emitted light is chromatically separated by a monochromator (NEWPORT cornerstone CS260), filter wheels (NEWPORT CS260 & THORLABS FW102C), and several filters (WG280 | BG39 | GG435 + KG3 | OG590 | RG715 | Si | Ge). The monochromatic light is chopped up by an optical chopper (THORLABS Optical Chopper) at a frequency of approximately 11 Hz, in order to use the lock-in-technique and by that to enhance the signal-/noise-ratio. The chopped monochromatic light passes a focus-lens (quartz) and hits the sample surface inside a quartz-Cuvette, which is filled up with CCl_4 (carbon tetrachloride). Light absorbed by the sample leads to heat generation, which is transferred to the CCl_4 and changes its refractive index. The refractive index change is detected by using a laser (UNIPHASE diode-laser, 632 nm) that passes through the CCl_4 near the sample surface and a quadrant detector (HAMATSU Photonics S1557). The entire data and signals are measured and processed by several lock-in-amplifiers (Stanford Research Systems SR830 & SR850), a COM-BUS-System, an analog controller system (MAID), and an inhouse measurement software. The systemic background noise is measured and subtracted. Throughout this study, two different TiO_2 thicknesses were used: ∼10 nm thick layers for measuring the passivation, contact resistivity, and interface properties and ∼100 nm for the structural-chemical and optical analysis methods. It is noted that 10 nm TiO_2 is comparatively thick for a passivating contact; however, we want to focus here on the material properties (especially, the differences between the Ti precursors) and less on interfacial properties.

III. RESULTS AND DISCUSSION

A. Si surface passivation

In Fig. 1, S_{eff} of symmetrical 10 nm ALD TiO_2 on *n*-type FZ-Si as a function of cumulative forming gas anneal duration at 250 °C is shown. For the $TiCl_4$ precursor [Fig. 1(a)], the best passivation with 3.9 cm/s (and a surface saturation current density $J_{0s} = 24$ fA/cm^2) is achieved at 75 °C deposition temperature on RCA-last Si without any postdeposition anneal. For 150 °C on RCA-last Si, the passivation is still very good, but S_{eff} increases beyond 10 cm/s for higher deposition temperatures. On HF-last Si, the best S_{eff} is 8.0 cm/s ($J_{0s} = 53$ fA/cm^2), which is also achieved in the as-deposited state at 75 °C. However, for higher deposition temperatures on HF-last Si, the passivation quality deteriorates, whereby S_{eff} increases to near and/or above 100 cm/s. The very

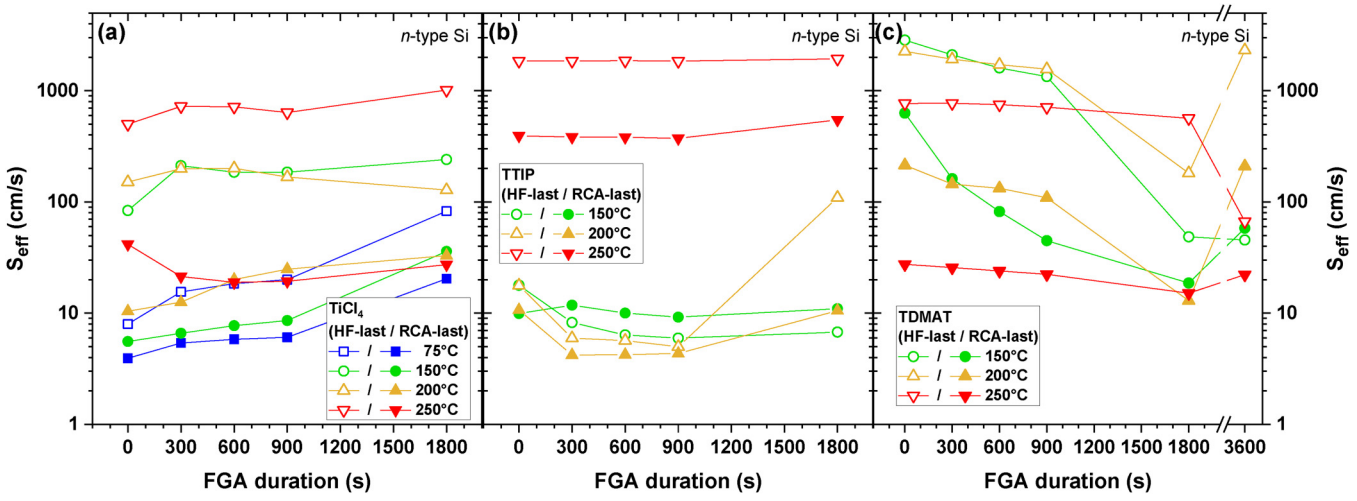

FIG. 1. Effective surface recombination velocity at an injection level of 10^{15} cm^{-3} of 10 nm ALD TiO_2 on *n*-type FZ-Si as a function of cumulative forming gas anneal duration at 250 °C. Panels (a)–(c) show the results for the ALD processes using $TiCl_4$, TTIP, and TDMAT, respectively. The data points at 0 s correspond to as-deposited samples. Open symbols indicate deposition on RCA cleaned substrates including the final HF dip. For the samples shown by the filled symbols, the interface oxide grown in the RCA-2 solution was still present.

good passivation quality of low-temperature-deposited (e.g., 75 °C) $TiCl_4$-TiO_2 does not benefit from an FGA, irrespective of the Si surface termination. Up to about 15 min FGA, S_{eff} increases just slightly before a more severe deterioration of the passivation quality occurs for longer anneals.

For the TTIP precursor [Fig. 1(b)], an S_{eff} of ~10 cm/s is observed in the as-deposited state on RCA-last Si for 150 and 200 °C, which approximately doubles for HF-last Si, indicating that the interfacial oxide benefits the passivation quality. FGA from 5 to 15 min tend to improve the passivation quality, with best results of 4.2 cm/s ($J_{0s} \approx 37$ fA/cm^2) achieved for RCA-last Si deposited at 200 °C. Hence, in contrast to $TiCl_4$, the TTIP process provides a Si surface passivation that is less sensitive to the Si pretreatment and that benefits from a short postannealing at 250 °C.

The TDMAT precursor was not found to provide comparably excellent Si surface passivation quality compared to $TiCl_4$ and TTIP precursors, as shown in Fig. 1(c). Although the RCA-last Si surface surpasses the HF-last surface, consistent with the $TiCl_4$ and TTIP precursors, no deposition temperature or FGA duration is capable to provide ≤10 cm/s. In this case, the best S_{eff} results of 13–19 cm/s ($J_{0s} = 51$–108 fA/cm^2) were found for RCA-last samples after 30 min FGA at 250 °C. The proportionality of the deposition temperature and S_{eff} observed for the other two Ti precursors is inverted for TDMAT so that better passivation is achieved for the highest temperatures. In contrast to TTIP, the RCA-2 grown interface SiO_x appears mandatory for a reasonable passivation using TDMAT since on the H-terminated Si surfaces only recombination velocities ≥50 cm/s were found even for long FGAs.

The same measurements on *p*-type FZ-Si are shown in Fig. 2 and the key findings from Fig. 1 using *n*-type silicon, whereby the lowest S_{eff} values are achieved for either the 75 °C-$TiCl_4$ process without FGA on RCA-last Si or the 200 °C-TTIP process with a 5–15 min FGA for both Si surface pretreatments. For $TiCl_4$ [Fig. 2(a)], the drawbacks of an H-terminated Si surface, higher deposition temperatures, and a postdeposition anneal at 250 °C are more clearly pronounced than on *n*-type Si. Altogether, it can be concluded that the best ALD TiO_2 process parameters and Si pretreatments provide a similarly excellent passivation quality on both *n*- and *p*-type Si surfaces.

B. Contact resistivity

The contact resistivity properties of the comparatively thick 10 nm TiO_2 layers are shown in Fig. 3. Each Ti precursor sample batch was FGA-annealed at 250 °C according to the best typical passivation qualities, i.e., $TiCl_4$: no FGA (as-deposited), TTIP: 15 min, TDMAT: 30 min. Due to the thicknesses beyond the direct tunnelling regime, the TiO_2 conductivity itself contributes here significantly to the contact resistivity, which provides a comparison between the different ALD precursors and deposition temperatures. It turns out that ρ_c values from 1 to 10 Ω cm^2 were measured without any clear trends concerning the Ti precursor or the deposition temperature. These results should not be overinterpreted but might indicate that electrically neither the precursor nor the temperature have a significant impact on the contact resistivity. Consequently, the ALD process and Si pretreatment with the best passivation quality can be selected and subsequently engineered toward the thinnest possible film thickness, which is the key to a low contact resistivity (see, e.g., the strong TiO_2 thickness dependence of ρ_c in Ref. 9). Another important point is the possible reduction of the TiO_2 to an oxygen-deficient TiO_x at the metal interface,[8] which will influence both passivation quality and contact resistivity. From the results shown in Fig. 3, we cannot see any drastic differences in ρ_c that indicate a Ti precursor dependence of the O-deficient TiO_x formation.

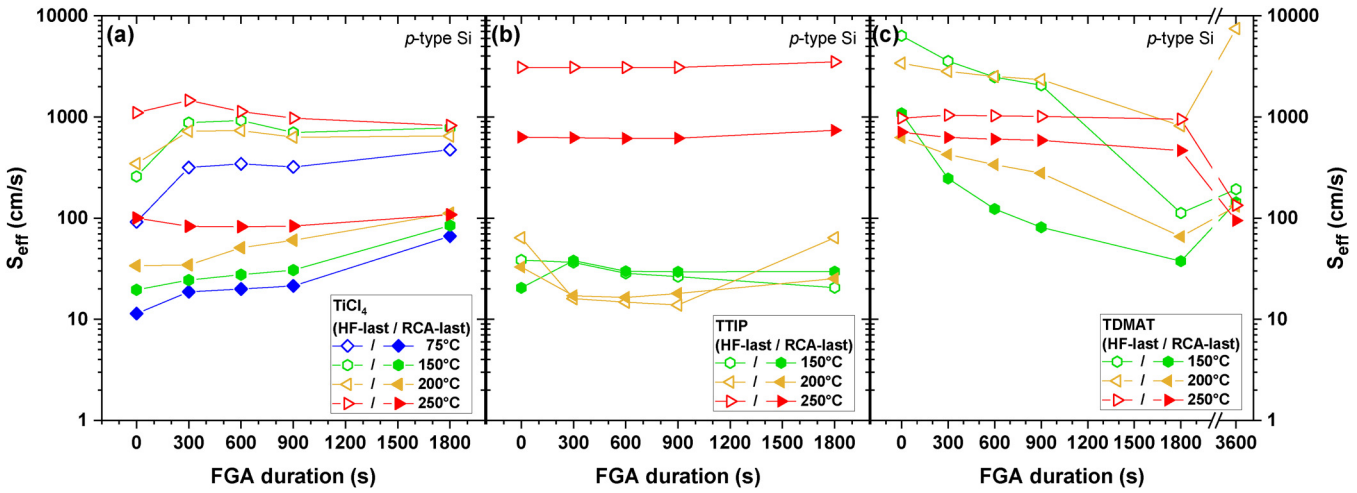

FIG. 2. Effective surface recombination velocity at an injection level of 10^{15} cm^{-3} of 10 nm ALD TiO_2 on *p*-type FZ-Si as a function of cumulative forming gas anneal duration at 250 °C. Panels (a)–(c) show the results for the ALD processes using $TiCl_4$, TTIP, and TDMAT, respectively.

C. Structural and compositional properties

In an attempt to explain the significant differences between the passivation quality of different ALD TiO_2 processes and to maximize its potential as surface passivation material, we investigate, in several different ways, the structural and compositional properties of ALD TiO_2 and its interface to the Si substrate.

In Fig. 4, the growth per cycle (GPC) values as determined by VASE of the thin and thick TiO_2 films made by the three different Ti precursors are shown. Since the deposition recipes were developed for thin films, all their thicknesses are (10 ± 1) nm. The linear extrapolation of the required cycle number for nominally ~100 nm thick films is, however, not straightforward for all samples, which results in a standard deviation of 27 nm for this sample batch. For $TiCl_4$, we find, besides an overall decreasing GPC with increasing deposition temperature, a GPC offset of on average ~0.14 Å between thin and thick films, which is related to an initial growth inhibition on the Si–H-terminated surface after the HF dip. Generally, for very thin TiO_2 layers, such as passivating contacts, the GPC differences between initial and steady-state growth as well as the difference between hydrophobic (HF-last) and hydrophilic (hydroxylated) Si surfaces have to be considered, which requires individual thickness determination. For TTIP, the GPC of thin films is approximately constant with deposition temperature, whereas for thicker films, we observe a slight increase in GPC. Instead, a significant GPC offset between thin and thick films appears for higher deposition temperatures. The high GPC values of $TiCl_4$ and TTIP at 250 °C are related to the crystallization of the TiO_2 films during deposition (cf. Raman data below), which is known to cause a GPC increase.[43,44] For TDMAT, the GPC decreases with increasing deposition temperature and is generally smaller for the thick samples, although the very small GPC of the thick TDMAT-250 samples is misleading here due to its severe non-stoichiometry (cf. ERDA data below). Overall, low- to medium-temperature ALD TiO_2 using $TiCl_4$ and TDMAT allows for efficient deposition with around 0.5 Å/cycle, whereas TTIP reaches just half of this GPC.

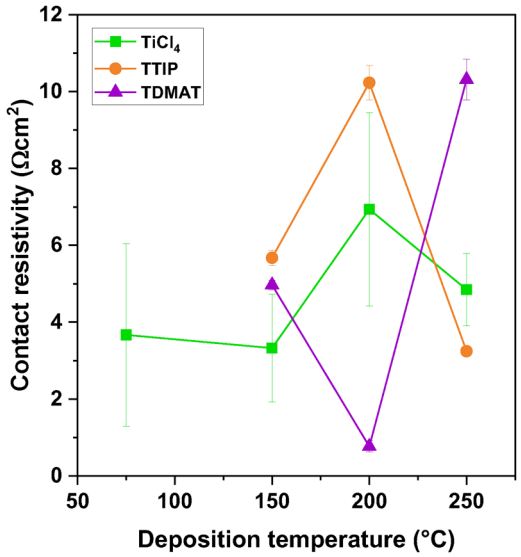

FIG. 3. Contact resistivities of 10 nm ALD TiO_2 on HF-last *n*-type Si as a function of deposition temperature using three different Ti precursors. Due to the thick layers, the TiO_2 conductivity has significant influence on the absolute ρ_c values.

The dispersions of the refractive index and the extinction coefficient extracted from the extended Cauchy model of VASE measurements between 400 and 1000 nm are shown in Figs. 5(a) and 5(b), respectively. All refractive indices at 633 nm are between 2.41 and 2.46 without any temperature or precursor trend, except for samples $TiCl_4$-75 and TTIP-150, which are slightly offset to lower

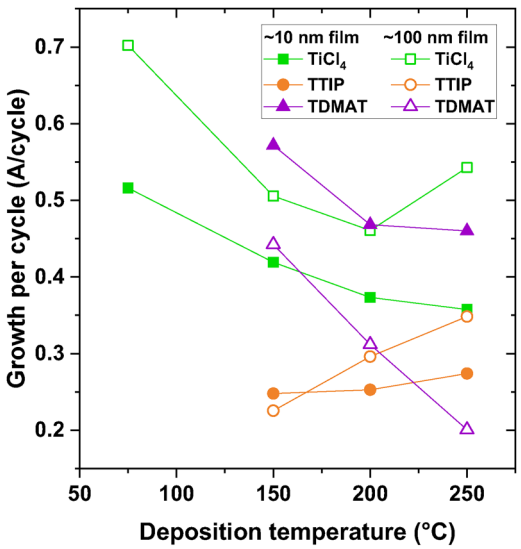

FIG. 4. Growth per cycle (GPC) as a function of deposition temperature on HF-last Si for the thin and thick TiO_2 films grown using three different Ti precursors.

n values (2.30). The severe nonstoichiometry of the thick TDMAT-250 sample causes a non-TiO_2-like dispersion.

The dispersions of the extinction coefficient [Fig. 5(b)] demonstrate the transparency of ALD TiO_2 over the relevant light spectrum. As a general trend, low deposition temperatures (75–150 °C) allow for optical transmittance (T) values of ~99% at 400 nm (violet light) even for the ~100 nm thick films, whereas the transmittance drops to near ~90% at 400 nm for 250 °C deposition temperature, which coincides with the anatase crystallization (cf. Raman data below). Whereas the *k*-dispersion of the thick $TiCl_4$-200 samples is either a problem of this specific sample or a fitting artifact, the low transmittance of just 56% at 400 nm of sample TDMAT-250 is related to its compositional Ti excess.

Due to the limited sensitivity of VASE to weakly absorbing defect states deeper in the TiO_2 bandgap, PDS was measured on the nominally 100 nm thick $TiCl_4$ and TTIP samples on quartz glass substrates. As shown in Fig. 6, all spectra show the same trends, i.e., E04-bandgaps in the range of 3.33–3.40 eV, an equal distribution of absorbing tail states at around 3 eV, and a rather flat, feature-less absorption spectrum for <3 eV. One exception is a very faint feature at ~2 eV for the sample TTIP-150, but we cannot extract any precise information due to the noise level in the weak absorption range of ~500 cm^{-1}. Importantly, we did not measure PDS to determine any parasitic absorption of sun light by TiO_2 passivating contacts but as an indication for optical transitions of defect states in the bandgap of TiO_2. Based on the PDS results, a significant density of such defect states in $TiCl_4$- and TTIP-based TiO_2 can be excluded.

In summary, the optical properties of ALD TiO_2 providing good Si surface passivation are equal with negligibly small parasitic light absorption. Hence, from a transparency point of view, ALD

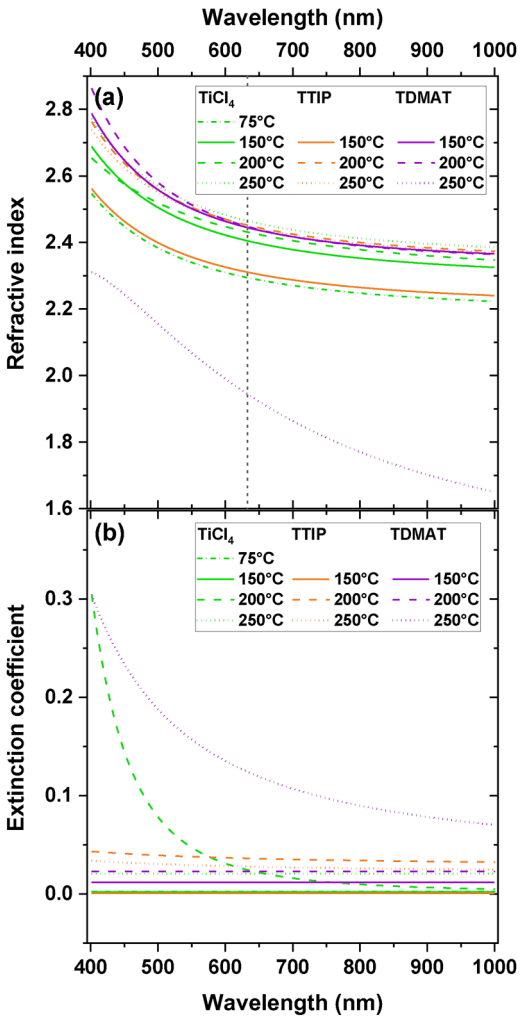

FIG. 5. (a) Dispersion of the refractive index (*n*) over the nominally transparent spectral range of the thick ALD TiO_2 samples. The dashed vertical line indicates the typical reference wavelength of 633 nm. (b) Dispersion of the extinction coefficient (*k*) of the same samples.

TiO_2 thin films are also compatible with an application as front-side contact or in bifacial solar cell designs, especially when considering only few nm thick films as required for passivating contacts.

The composition of all ~100 nm thick ALD TiO_2 samples as measured by ERDA is shown in Fig. 7. The Ti and O concentrations are shown in Fig. 7(a), and their ratio (stoichiometry) is plotted in Fig. 7(b). Within error bars, the samples can be considered stoichiometric with a [O]/[Ti] ratio of ~2, with the exception of TDMAT-250. A general slight overstoichiometry of up to 2.1 has been reported before for ALD TiO_2.[5] Although the optical and structural results of the 10 nm TDMAT-250 sample are all fine, some degradation of the layer composition must have happened during the deposition of the ~100 nm thick films, which was

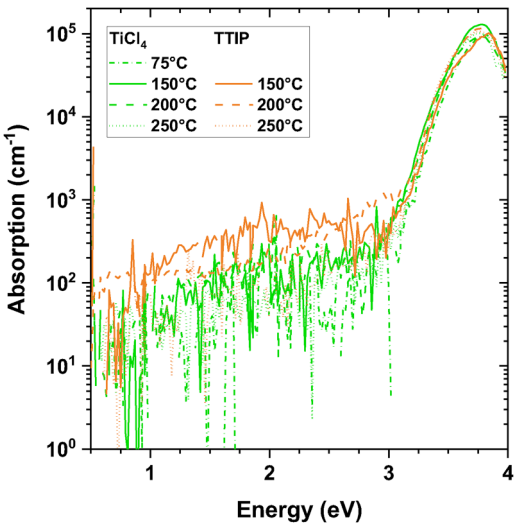

FIG. 6. PDS absorption spectra of the thick ALD TiO_2 films fabricated by $TiCl_4$ and TTIP precursors on quartz glass.

accompanied by a Ti excess (also visible to some extent for the thick TDMAT-200 sample).

Hydrogen [Fig. 7(c)] is one of the dominating impurity elements in all films, especially for low deposition temperatures, and the crucial role of H in ALD passivation materials is well established. However, there are severe differences between the Ti precursors, e.g., for 150 °C deposition temperature, H-concentrations from 9.15 at. % (TTIP) to 0.72 at. % ($TiCl_4$) are measured, although both provide very good passivation qualities. The lack of [H] in $TiCl_4$-150 might be compensated by additional 2.28 at. % of chlorine [cf. Fig. 7(d)], which supports the idea of Cl-impurities passivating defects at the Si/SiO_x:TiO_2 interface.[45,46] Consequently, the samples $TiCl_4$-75, which contain [Cl] = 5.86 at. % and [H] = 4.72 at. % achieve the lowest S_{eff} values. Furthermore, we observed that the very good passivation supported by Cl does not require any thermal activation by postdeposition annealing ($TiCl_4$), in contrast to the interface defect passivation by H (TTIP). Hence, it appears that low- and medium-temperature $TiCl_4$-TiO_2 passivates the Si surface very well in the as-deposited state due to [Cl] and [H], whereas medium-temperature TTIP-TiO_2 passivates based on [H], which requires thermal activation.

The generally smaller [H]-concentrations of the TDMAT samples (combined with the absence of chlorine) can explain why the Si surface passivation quality in the as-deposited state is inferior. In contrast to typical ALD materials where the interface passivating hydrogen originates from the layer material itself,[47] it is possible that hydrogen from the gaseous atmosphere diffuses toward the interface during the long FGAs required to activate the passivation of the TMDAT samples.

Carbon impurities from the metalorganic precursors [Fig. 7(d)] are only significant for sample TTIP-150 with 1.91 at. % and generally much lower for TDMAT (beyond detection limit for TDMAT-250). Carbon seems to have neither a beneficial nor a detrimental impact on the Si surface passivation.

A compositional XPS analysis of the nominal 10 nm ALD TiO_2 films (without any postannealing) is shown in Fig. 8. The normalized and stacked Ti 2p spectra with their spin–orbit components Ti $2p_{3/2}$ and Ti $2p_{1/2}$ are shown. For all samples, the peaks are located in a narrow range of 458.5–458.8 eV (Ti $2p_{3/2}$) and 464.2–464.6 eV (Ti $2p_{1/2}$), which corresponds to the Ti^{4+} oxidation state. Within these small energy windows, there are no systematic shifts of the Ti^{4+} binding energies that could be correlated to the deposition temperature or the Ti precursor. Even for the very low deposition temperature of only 75 °C ($TiCl_4$-75), no suboxide shoulders at lower binding energies are observed. Cumulative peak fits of selected samples that illustrate this observation are shown in Fig. S1 in the supplementary material. It is concluded that all ALD recipes resulted in thin films (here ~10 nm) of stoichiometric TiO_2 so that the differences in the passivation quality cannot be related to the TiO_2 volume itself. Within the typical XPS analysis depth of ~5 nm, we probe approximately the upper half of the 10 nm thin film. Hence, differences in the initial growth such as mixed SiO_x-TiO_x near-interfacial layers[19] are not detected. This highlights the importance of the Si substrate pretreatments and the first ALD cycles since the TiO_2 grown in the steady-state is apparently very similar in its stoichiometry and bonding configuration for all precursors and temperatures. Furthermore, it is noted that the strongly nonstoichiometric composition measured by ERDA for TDMAT-250 is an artifact of that thick film deposited for specific measurement methods, which may have occurred during the long deposition time.

Raman spectroscopy was used to investigate the crystallinity of the ~100 nm thick as-deposited ALD TiO_2 films. The results are shown in Fig. 9. Samples TTIP-250, TTIP-200, and $TiCl_4$-250 show clear peaks at 143, 197, 397, 516, and 639 cm^{-1}, which correspond to the TiO_2 polymorph anatase. Weak crystalline features especially at 143 cm^{-1} can be found for $TiCl_4$-200 and TDMAT-200, which indicates the onset of crystallization. We refrain from overinterpreting the Raman spectrum of sample TDMAT-250 since the absence of clear crystalline peaks might be simply caused by the nonstoichiometry of this sample. A purely amorphous morphology is only found for samples deposited at 75 and 150 °C (irrespective of the Ti precursor used). Nevertheless, prior work has shown that in situ crystallization of ALD TiO_2 films during deposition are a function of both temperature and thickness.[43,48,49] However, samples TTIP-200 (fully crystalline) and $TiCl_4$-200 (only one weak crystalline Raman peak) also demonstrate that the Ti precursor, the GPC, or the deposition time at a given temperature (here ~1 h for the $TiCl_4$ sample versus ~8h for the TTIP sample) may play a role in the crystallization of the TiO_2 films. Since amorphous ALD TiO_2 provides better Si surface passivation qualities than polycrystalline films,[5,50] crystallization should be avoided by using low deposition temperatures (≤150 °C), faster ALD recipes with preferably high GPC ($TiCl_4$-recipes), and not too thick TiO_2 films (≪100 nm).

D. Effective charge density Q_f

In order to ascertain the magnitude of fixed charge density within the TiO_2 films, we have modelled the injection-dependent

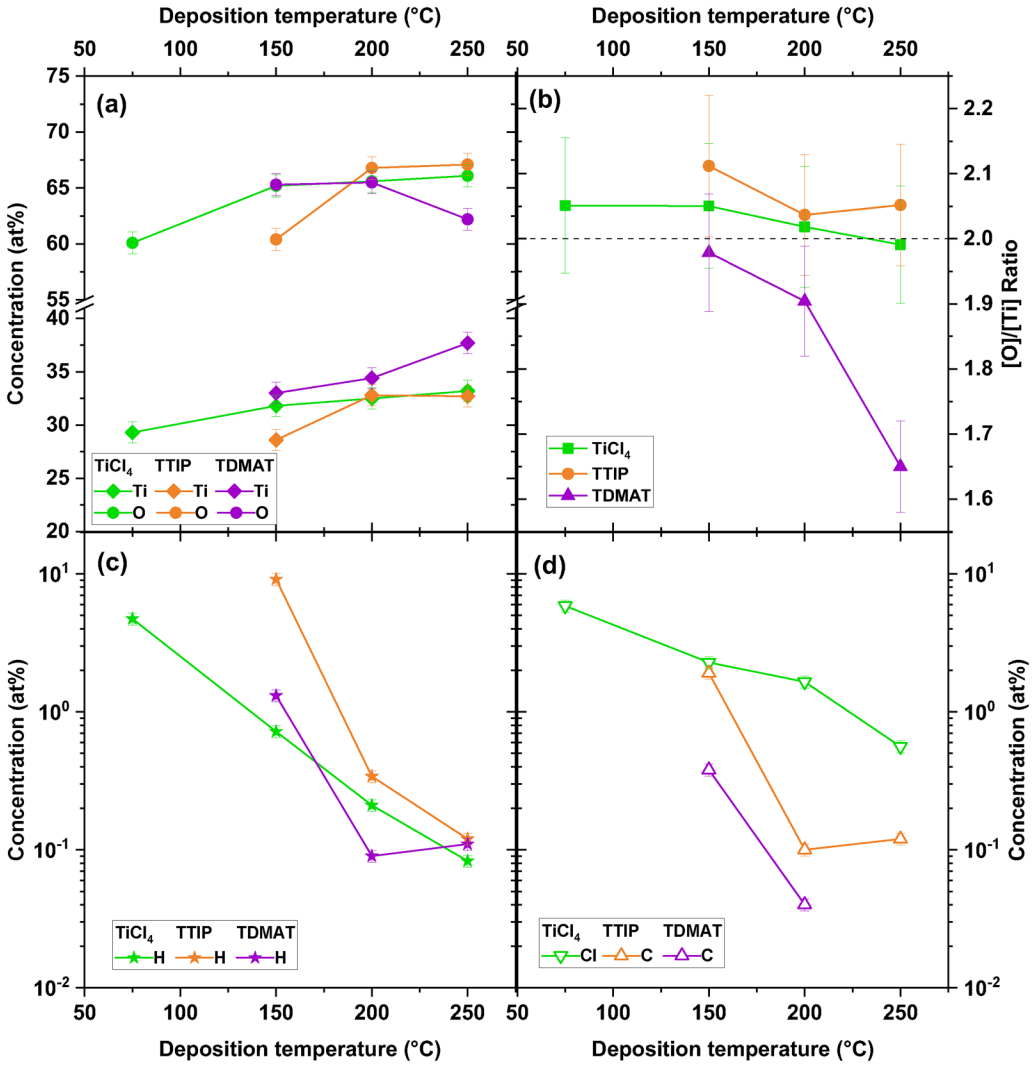

FIG. 7. Composition and impurity concentrations of the nominally ~100 nm thick ALD TiO_2 samples as determined by ERDA: (a) titanium and oxygen concentrations, (b) stoichiometry as [O]/[Ti] ratio whereby the horizontal dashed line indicates the ideal TiO_2 stoichiometry of 2, (c) hydrogen impurities, and (d) chlorine or, respectively, carbon impurities.

effective lifetime curves, with results presented in Fig. 10. For clarity, Fig. 10 only shows the modeling for some of the highest effective lifetimes achieved for each of the different precursors; TTIP (HF last) deposited at 200 °C and with a 10 min FGA, TiCl (RCA last) deposited at 75 °C without an FGA, and TDMAT (RCA last) deposited at 150 °C and with and without a 10 min FGA. To demonstrate that the lifetime curves presented in Fig. 10 are not limited by bulk recombination, Fig. 10(a) plots the effective lifetime of a sister sample that underwent a superacid based treatment.[31,37,38] As can be seen in Fig. 10(a), the effective lifetime of the superacid treated sample is well in excess of 10 ms for injection levels $>10^{15}$ cm^{-3}, implying bulk recombination is not limiting the effective lifetime when the silicon samples are passivated with TiO_2. As such, we can infer from this result that our TiO_2 passivated samples are primarily limited by surface recombination.

In Fig. 10(a), we show that a fixed charge density on the order of $\sim 10^{11}$ qcm^{-2} best fits the lifetime curve, while for much higher values of Q_f (e.g., $>-5.0 \times 10^{11}$ qcm^{-2}), a much steeper increase in lifetime (between Δn of 10^{14} and 10^{16} cm^{-3}) is observed, while for very low Q_f values, the increase in lifetime between Δn of 10^{14} and 10^{16} cm^{-3} is shallow. The steepness of the lifetime in our case is, thus, controlled by which passivation mechanism is more dominant, e.g., chemical or field-effect passivation. Looking at Figs. 10(b) and 10(c), we observe a similar finding, whereby very high Q_f values cannot accurately fit the lifetime curves. In fact, we observe the opposite trend, whereby lower values of Q_f are found to more

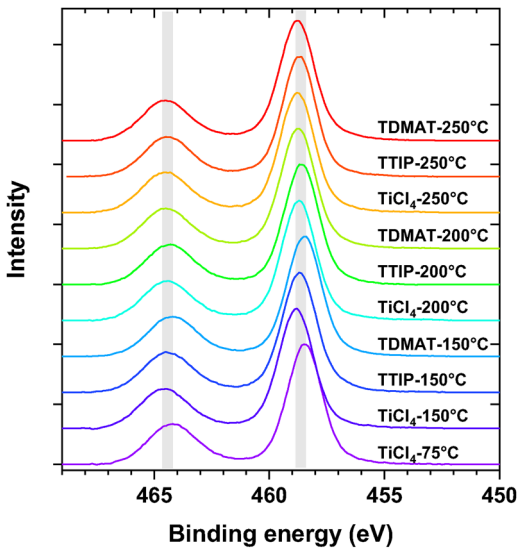

FIG. 8. XPS Ti 2p spectra of as-deposited, thin ALD TiO_2 films on HF-last *n*-type Si. The vertical gray lines indicate the Ti $2p_{3/2}$ (~458.7 eV) and Ti $2p_{1/2}$ (~464.4 eV) peaks characteristic for the Ti^{4+} oxidation state.

accurately fit the experimental lifetime curves, thus implying chemical passivation is relatively high for our TiO_2-passivated samples. Therefore, although we cannot ascertain correlations in Q_f with the type of Ti precursor, surface preconditioning, deposition temperature, or postdeposition anneal time, we can infer that

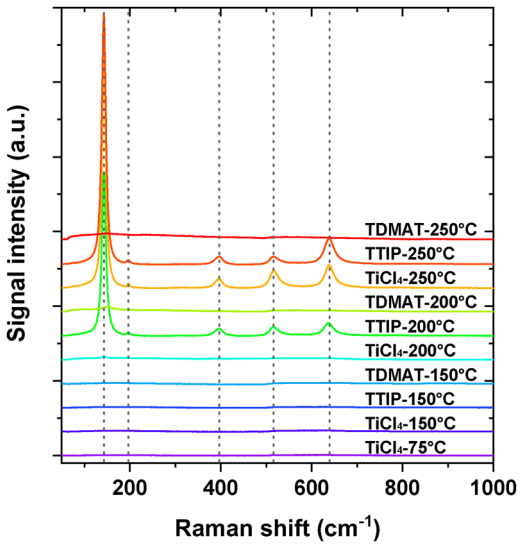

FIG. 9. Raman spectra of as-deposited ALD TiO_2 on quartz glass substrates. The vertical dashed lines indicate the typical peaks of the anatase crystal structure.

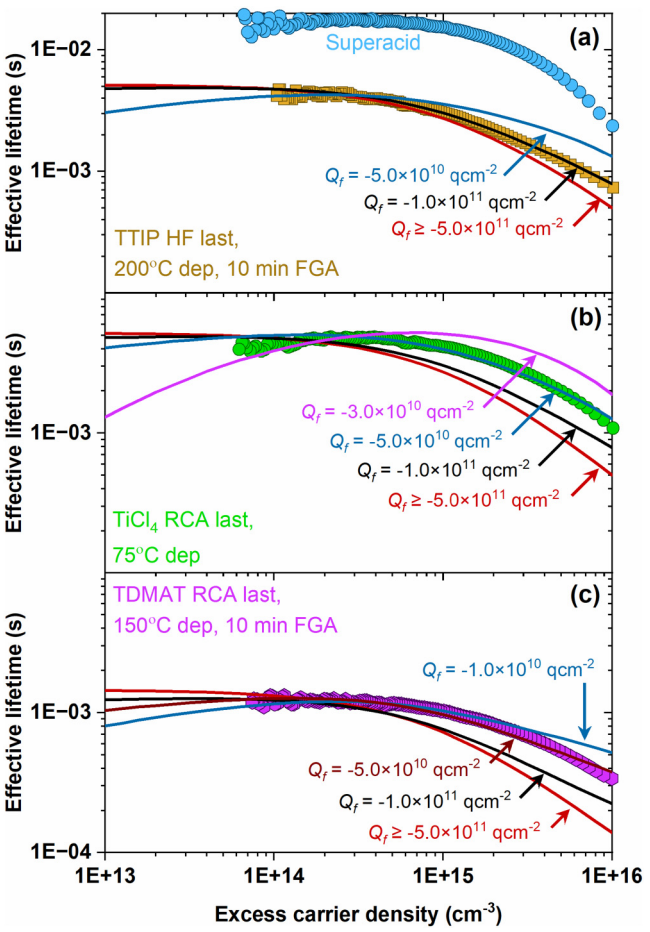

FIG. 10. Injection-dependent effective lifetime curves of TiO_2 passivated silicon for (a) TTIP (HF last) deposited at 200 °C and with a 10 min FGA, (b) $TiCl^4$ (RCA last) deposited at 75 °C without an FGA, and (c) TDMAT (RCA last) deposited at 150 °C and with a 10 min FGA. The circles in (a) correspond to the measured effective lifetime for a superacid-treated silicon sample. The solid lines in all figures correspond to the modelled effective lifetime with different levels of negative fixed charge (lower limit only).

our ALD TiO_2 films do not likely possess very high levels of fixed charge (e.g., $> -10^{12}$ qcm^{-2}) as seen for other dielectric films such as Al_2O_3 and HfO_2.[51,52] We note, however, that our modeling assumes a single energy level defect at midgap, the bulk lifetime does not vary between samples, and that edge recombination is neglected (because the edges were passivated), meaning the values of Q_f modelled in this work should be considered as a lower limit only.

E. Interfacial SiO_x

H-concentration and effective charge density give rise to chemical and field effect passivation, respectively. However, the chemical passivation is also ruled by the ultrathin interfacial SiO_x

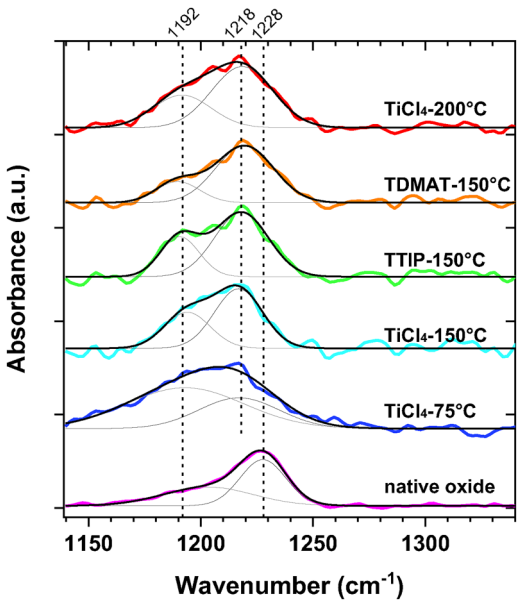

FIG. 11. FTIR spectra of nominally 10 nm ALD TiO_2 on HF-last Si (no postannealing) in the region of symmetric Si–O stretching mode together with cumulative peak fits using two Gaussian functions.

or SiO_x-TiO_x layer that separates the TiO_2 from the Si. Unless intentionally grown before the ALD process (e.g., the RCA-last samples in this study or demonstrated in Refs. 8–10, 12, and 22), the SiO_x and SiO_x-TiO_x form during the initial ALD cycles. Here, we use polarized Brewster-angle reflection FTIR on selected 10 nm ALD TiO_2 (as-deposited) on HF-last Si to investigate differences in the interface oxide caused by the different Ti precursors. As shown recently for ALD Al_2O_3, this specific FTIR method is highly sensitive to the LO phonon modes of the symmetric Si–O stretching vibration.[42,51] The FTIR spectra are shown in Fig. 11.

For all ALD TiO_2 samples, the cumulative peak fit with two Gaussians reveals one peak at around 1218 cm^{-1} related to interfacial SiO_x that dominates the spectrum for all but sample $TiCl_4$-75 (blue curve). For the native oxide reference sample (purple curve), the dominating peak is shifted to 1228 cm^{-1}. Please note that the native oxide used here is an out-of-box Si sample, i.e., the wafer surface was exposed to ambient air conditions for a very long time. The significantly higher wavenumber (frequency) indicates a higher stoichiometry and density of the native oxide compared to the interfacial SiO_x grown by the ALD TiO_2 process. In the literature, LO peaks of interfacial SiO_x underneath ALD Al_2O_3 on Si were observed by Lee *et al.* at 1221 cm^{-1} for thermal ALD on HF-last and RCA-last Si[42] and at 1223 cm^{-1} for nonannealed plasma-enhanced ALD samples.[53] The authors showed that annealing at 450 °C shifts this peak up to 1244 cm^{-1}, which is accompanied by an increased atomic density of 2.57×10^{22} cm^{-3}.[53] In contrast, a 1.3 nm-thick SiO_x from nitric acid oxidation (NAOS) with an LO peak at 1219 cm^{-1} was reported to have a density of only 2.20×10^{22} cm^{-3}.[54] Hence, the interfacial SiO_x between HF-last Si and thermal ALD TiO_2 appears to be more comparable to NAOS oxides rather than to the density and stoichiometry of, e.g., SiO_x grown by ALD Al_2O_3 processes or the native oxide. When comparing the height of the 1218 cm^{-1} peaks in Fig. 11 with the passivation qualities, no correlation is found.

A second peak at lower wavenumbers causes a shoulder of the SiO_x LO-mode. For all TiO_2 samples, it occurs at around 1192 cm^{-1}, whereas for the native oxide reference it occurs at 1203 cm^{-1} and is very weak. No peak at 1192 cm^{-1} was observed for various ALD Al_2O_3 layers on Si, but a weak feature at around 1203 cm^{-1} that contributes to an overall peak broadening could be present in the thermal ALD and as-deposited samples shown in Refs. 42 and 53 If the 1203 cm^{-1} peak represents a silicon suboxide mode in the interfacial SiO_x layer, the shift to lower wavenumbers (i.e., 1192 cm^{-1}) indicates that an increased mass is involved in this vibration. Here, heavy Ti atoms are likely to be incorporated into the SiO_x-network so that the 1192 cm^{-1} peak would represent the IR-mode of the Si–O–Ti bonds identified by Dwivedi *et al.* using XPS and electron energy loss spectroscopy.[19] Comparing the height of the 1192 cm^{-1} peaks in Fig. 11 with the surface passivation qualities on HF-last Si (open symbols in Fig. 1), some anticorrelation can be found, i.e., the higher the 1192 cm^{-1} peak, the lower S_{eff}. This suggests that interfacial SiO_x-TiO_x mixed oxides are beneficial for the passivation quality.

IV. SUMMARY AND CONCLUSIONS

The Si surface passivation quality of ALD TiO_2 grown by the precursors $TiCl_4$, TTIP, and TDMAT was studied. Using a suitable combination of Si pretreatment, ALD, and postdeposition processing, some TiO_2 thin films provide very low S_{eff}. The origin of the partially excellent Si surface passivation by ALD TiO_2 appears to be a complex combination of different parameters since neither low deposition temperature, nor high concentration of H or Cl, nor high effective charge densities, nor a certain interface SiO_x alone determine S_{eff}. Severe differences in S_{eff} are found for HF-last versus RCA-last Si-surfaces: For $TiCl_4$-based TiO_2, the wet chemically grown SiO_x interface layer seems to be decisive for the passivation, whereas the isopropoxide groups in TTIP apparently grow their own high-quality SiO_x on the H-terminated Si surface. A high initial H-concentration is not a guarantor for very low surface recombination *per se* (cf. the two well-passivating layers $TiCl_4$-150 and TTIP-150 with their H-concentration difference of a factor of ~13). Specifically for low-temperature depositions of $TiCl_4$-TiO_2, several at. % of Cl appear to have a highly beneficial impact on S_{eff}, which—in contrast to passivating H—requires apparently no thermal activation by a postdeposition anneal. The passivation of dangling bonds at the Si/SiO_x-TiO_x interface by Cl-impurities from the $TiCl_4$ precursor *during* the deposition could explain why $TiCl_4$-TiO_2 passivates already excellently in the as-deposited state, whereas the dangling bond passivation by H from TTIP-TiO_2 requires a post-deposition treatment. Most recently, the role of chlorine in the Si surface passivation by $TiCl_4$-TiO_2 was also highlighted in Ref. 46. The absence of Cl-impurities and the low H-concentration of TDMAT-TiO_2 gives rise to an inferior surface passivation irrespective of a postanneal. A small to medium concentration of negative fixed charges is found for all ALD TiO_2 layers, giving rise to an

additional field-effect passivation component. Since no correlation is found between the Cl-impurity concentration and the negative effective charge, Cl can be ruled out as origin of Q_f in ALD TiO_2.

In summary, ALD TiO_2 grown by $TiCl_4$ and H_2O appears to be superior for Si surface passivation and as electron-selective contact over the other Ti precursors (TTIP, TDMAT) for several reasons: (i) it allows for very low S_{eff} to be achieved without the need of an additional postdeposition anneal, most likely due to chlorine impurities, (ii) the GPC of the $TiCl_4$ process is at least twice as high as compared to the TTIP process but similar to TDMAT, and (iii) the $TiCl_4$ precursor does not require any heating to draw vapor from the precursor cylinder during ALD pulsing. Finally, both $TiCl_4$ and TTIP are rather cheap precursors in contrast to TDMAT.

ACKNOWLEDGMENTS

D.H. acknowledges funding via a DFG-Heisenberg Grant (No. 434030435). Parts of this research work were accomplished by D.H. in the PV-Labs at ANU during a Feodor Lynen Fellowship and at IHM, TU Dresden during a Feodor Lynen Return Fellowship, for which the Alexander von Humboldt Foundation (AvH) as well as both host institutions are gratefully acknowledged. Furthermore, D.H. acknowledges funding from the Australian Centre for Advanced Photovoltaics (ACAP, Collaboration Grant). In this study, ellipsometer facilities at the ACT Node of the Australian National Fabrication Facility (ANFF) were used. Parts of this research were carried out at the Ion Beam Center at the Helmholtz-Zentrum Dresden-Rossendorf e.V., a member of the Helmholtz Association.

AUTHOR DECLARATIONS

Conflict of Interest

The authors have no conflicts to disclose.

Author Contributions

Daniel Hiller: Conceptualization (lead); Data curation (supporting); Investigation (lead); Supervision (lead); Writing – original draft (lead); Writing – review & editing (equal). **Frans Munnik:** Data curation (supporting); Writing – review & editing (supporting). **Julian López-Vidrier:** Data curation (supporting); Writing – review & editing (supporting). **Dmytro Solonenko:** Data curation (supporting); Writing – review & editing (supporting). **Johanna Reif:** Data curation (supporting). **Martin Knaut:** Data curation (supporting); Writing – review & editing (supporting). **Oliver Thimm:** Data curation (supporting); Writing – review & editing (supporting). **Nicholas E. Grant:** Data curation (supporting); Writing – review & editing (equal).

DATA AVAILABILITY

The data that support the findings of this study are available from the corresponding author upon reasonable request.

REFERENCES

[1]A. Blakers, M. Stocks, B. Lu, C. Cheng, and R. Stocks, IEEE J. Photovolt. **9**, 1828 (2019).
[2]A. Blakers, IEEE J. Photovolt. **9**, 629 (2019).
[3]S. W. Glunz and F. Feldmann, Sol. Energy Mater. Sol. Cells **185**, 260 (2018).
[4]A. Cuevas, Y. Wan, D. Yan, C. Samundsett, T. Allen, X. Zhang, J. Cui, and J. Bullock, Sol. Energy Mater. Sol. Cells **184**, 38 (2018).
[5]B. Liao, B. Hoex, A. G. Aberle, D. Chi, and C. S. Bhatia, Appl. Phys. Lett. **104**, 253903 (2014).
[6]J. Cui *et al.*, Sol. Energy Mater. Sol. Cells **158**, 115 (2016).
[7]B. Liao, B. Hoex, K. D. Shetty, P. K. Basu, and C. S. Bhatia, IEEE J. Photovolt. **5**, 1062 (2015).
[8]X. Yang, Q. Bi, H. Ali, K. Davis, W. V. Schoenfeld, and K. Weber, Adv. Mater. **28**, 5891 (2016).
[9]X. Yang, P. Zheng, Q. Bi, and K. Weber, Sol. Energy Mater. Sol. Cells **150**, 32 (2016).
[10]V. Titova, B. Veith-Wolf, D. Startsev, and J. Schmidt, Energy Proc. **124**, 441 (2017).
[11]T. G. Allen *et al.*, Adv. Energy Mater. **7**, 1602606 (2017).
[12]T. Mochizuki, K. Gotoh, Y. Kurokawa, T. Yamamoto, and N. Usami, Adv. Mater. Interfaces **6**, 1801645 (2019).
[13]Y. Nakagawa, K. Gotoh, T. Inoue, Y. Kurokawa, and N. Usami, Phys. Status Solidi A **218**, 2100296 (2021).
[14]T. Matsui, M. Bivour, P. Ndione, P. Hettich, and M. Hermle, Energy Proc. **124**, 628 (2017).
[15]T. Matsui, S. McNab, R. S. Bonilla, and H. Sai, ACS Appl. Energy Mater. **5**, 12782 (2022).
[16]W. Liang *et al.*, Phys. Status Solidi RRL **17**, 2200304 (2023).
[17]M. M. Shehata, G. Bartholazzi, D. H. Macdonald, and L. E. Black, Adv. Energy Mater. **13**, 2300251 (2023).
[18]H. Shen *et al.*, Sci. Adv. **4**, eaau9711 (2018).
[19]N. Dwivedi, R. J. Yeo, H. R. Tan, R. Stangl, A. G. Aberle, C. S. Bhatia, A. Danner, and B. Liao, Adv. Funct. Mater. **28**, 1707018 (2018).
[20]A. Stesmans, J. Appl. Phys. **88**, 489 (2000).
[21]Y. Nakagawa, K. Gotoh, M. Wilde, S. Ogura, Y. Kurokawa, K. Fukutani, and N. Usami, J. Vac. Sci. Technol. A **38**, 022415 (2020).
[22]K. Gotoh, T. Mochizuki, T. Hojo, Y. Shibayama, Y. Kurokawa, E. Akiyama, and N. Usami, Curr. Appl. Phys. **21**, 36 (2021).
[23]T. Matsui, M. Bivour, P. F. Ndione, R. S. Bonilla, and M. Hermle, Sol. Energy Mater. Sol. Cells **209**, 110461 (2020).
[24]J. P. Niemelä, G. Marin, and M. Karppinen, Semicond. Sci. Technol. **32**, 093005 (2017).
[25]M. M. Plakhotnyuk, N. Schüler, E. Shkodin, R. A. Vijayan, S. Masilamani, M. Varadharajaperumal, A. Crovetto, and O. Hansen, Jpn. J. Appl. Phys. **56**, 08MA11 (2017).
[26]T. Matsui, M. Bivour, M. Hermle, and H. Sai, ACS Appl. Mater. Interfaces **12**, 49777 (2020).
[27]T. Mochizuki, K. Gotoh, A. Ohta, S. Ogura, Y. Kurokawa, S. Miyazaki, K. Fukutani, and N. Usami, Appl. Phys. Express **11**, 102301 (2018).
[28]G. Dingemans and W. M. M. Kessels, ECS Transact. **41**, 293 (2011).
[29]F. E. Rougieux, N. E. Grant, C. Barugkin, D. Macdonald, and J. D. Murphy, IEEE J. Photovolt. **5**, 495 (2015).
[30]N. E. Grant, V. P. Markevich, J. Mullins, A. R. Peaker, F. Rougieux, and D. Macdonald, Phys. Status Solidi RRL **10**, 443 (2016).
[31]D. Hiller *et al.*, Phys. Status Solidi A **217**, 2000436 (2020).
[32]N. E. Grant, A. I. Pointon, R. Jefferies, D. Hiller, Y. Han, R. Beanland, M. Walker, and J. D. Murphy, Nanoscale **12**, 17332 (2020).
[33]See http://www.pvlighthouse.com.au for "Calculator map on PV Lighthouse" (accessed May 2021).
[34]R. B. M. Girisch, R. P. Mertens, and R. F. D. Keersmaecker, IEEE Trans. Electron Dev. **35**, 203 (1988).
[35]A. G. Aberle, S. Glunz, and W. Warta, J. Appl. Phys. **71**, 4422 (1992).

[36]T. Niewelt *et al.*, Sol. Energy Mater. Sol. Cells **235**, 111467 (2022).
[37]J. Bullock *et al.*, ACS Appl. Mater. Interfaces **8**, 24205 (2016).
[38]A. I. Pointon, N. E. Grant, E. C. Wheeler-Jones, P. P. Altermatt, and J. D. Murphy, Sol. Energy Mater. Sol. Cells **183**, 164 (2018).
[39]R. H. Cox and H. Strack, Solid-State Electron. **10**, 1213 (1967).
[40]K. Arstila *et al.*, Nucl. Instrum. Methods Phys. Res. Sect. B **331**, 34 (2014).
[41]N. P. Barradas, C. Jeynes, and R. P. Webb, Appl. Phys. Lett. **71**, 291 (1997).
[42]C. Y. Lee, S. Wang, X. Cui, T. Zhang, R. Deng, K. T. Khoo, and B. Hoex, Phys. Status Solidi RRL **12**, 1800156 (2018).
[43]G. Luka, B. S. Witkowski, L. Wachnicki, M. Andrzejczuk, M. Lewandowska, and M. Godlewski, Cryst. Eng. Comm. **15**, 9949 (2013).
[44]W. Chiappim, G. E. Testoni, J. S. B. de Lima, H. S. Medeiros, R. S. Pessoa, K. G. Grigorov, L. Vieira, and H. S. Maciel, Braz. J. Phys. **46**, 56 (2015).
[45]B. Liao, N. Dwivedi, Q. Wang, R. J. Yeo, A. G. Aberle, C. S. Bhatia, and A. Danner, IEEE J. Photovolt. **11**, 319 (2021).
[46]M. M. Shehata, D. H. Macdonald, and L. E. Black, ACS Appl. Mater. Interfaces **15**, 46504 (2023).
[47]M. Schnabel, B. W. H. Van De Loo, W. Nemeth, B. Macco, P. Stradins, W. M. M. Kessels, and D. L. Young, Appl. Phys. Lett. **112**, 203901 (2018).
[48]J. Aarik, A. Aidla, H. Mändar, T. Uustare, M. Schuisky, and A. Harsta, J. Cryst. Growth **242**, 189 (2002).
[49]D. Suh, D. Y. Choi, and K. J. Weber, J. Appl. Phys. **114**, 154107 (2013).
[50]W. Liang *et al.*, IEEE J. Photovolt. **10**, 940 (2020).
[51]S. L. Pain *et al.*, Adv. Mat. Interfaces **9**, 2201339 (2022).
[52]N. E. Grant *et al.*, Appl. Surf. Sci. **645**, 158786 (2024).
[53]C. Y. Lee, S. Deng, T. Zhang, X. Cui, K. T. Khoo, K. Kim, and B. Hoex, AIP Adv. **8**, 075204 (2018).
[54]X. Asuha, T. Yuasa, O. Maida, and H. Kobayashi, Appl. Phys. Lett. **80**, 4175 (2002).
[55]See supplementary material for x-ray photoelectron spectroscopy Ti-2p spectra of selected ALD-TiO_2 samples including cumulative peak fits.